Supplementary Information (SI) for Journal of Materials Chemistry A.

Supporting Information for:

Selective captivation of DOX via topotactic surface enrichment with hydrated sodium ions on engineered MXene nanosheets

Zubair Khalid,[1] Jing Xie,[1] Farhan Hadi,[1] Tetsuo Yamaguchi,[1,2] Fabrice Salles,[3*] Jae-Min Oh,[1*]*

[1]*Department of Energy and Materials Engineering, Dongguk University-Seoul, 04620, Seoul, Korea*

[2]*Department of Applied Chemistry for Environment, School of Biological and Environment Science, Kwansei Gakuin University, 669-1330, Hyogo, Japan*

[3]*Institute Charles Gerhardt Montpellier (ICGM), Université de Montpellier, CNRS, ENSCM, Montpellier, France*

E-mail: tetsuo.y@dgu.ac.kr (T. Yamaguchi)

E-mail: fabrice.salles@umontpellier.fr (F. Salles)

E-mail: jaemin.oh@dongguk.edu (J-. M. Oh)

Content list:

1. Experimental section

1.1 Materials

Titanium (Ti, 99.5%, metal basis), aluminum (Al, 99.5%, metal basis), and graphite powder (C, conducting grade, 99.5%, metal basis) were purchased from Alfa Aesar (Haverhill, Massachusetts, United States). Hydrofluoric acid (HF, 49%) was purchased from SAMCHUN (Daejon, Republic of Korea). Doxorubicin hydrochloride (DOX) was purchased from ChemScene (99.60%, NJ, USA). Pellet form of sodium hydroxide (NaOH) was obtained from DAEJUNG (Siheung, Republic of Korea). All the materials were used without further treatment.

1.2 Synthesis

1.2.1 Parent MAX phase: Ti_3AlC_2

For the preparation of parent MAX (Ti_3AlC_2), titanium, aluminum, and graphite powders were added to a manual ball mill equipped with yttrium stabilized zirconia balls in either stoichiometric (3:1:2) or modified ratios (3.2:1.8:2). The mixture was homogeneously mixed for 2 h manually. Then the mixture was transferred to an alumina crucible and located in a tube furnace of which the atmosphere was inertly controlled with an argon flow. The sample was heated to 1450°C with a temperature increasing rate of 5ºC/min and then maintained for 4 h. The furnace was cooled down to room temperature under ambient conditions. Then stoney mass-like solids were broken into small pieces and then crushed into fine particles using an agate mortar and a pestle.

1.2.2 Preparation of MXene: $Ti_3C_2T_x$

The MXene ($Ti_3C_2T_x$) was obtained by etching the Al layer selectively from MAX (the one prepared with modified ratio of 3.2:1.8:2) utilizing 40% HF. Typically, the MAX powder (1.00

g) was added slowly to a high-density polypropylene bottle containing 40% HF (50 mL) to avoid overheating. The cap of the bottle was connected to the overhead condenser to release gases and trap the HF vapor. The suspension was stirred at 400 rpm for 24 h at 60°C. Then, the suspension was centrifuged at 10,000 rpm for 25 min to separate a black filter cake, the exfoliated MXene. The black part was redispersed in deionized (DI) water and centrifuged again to wash out water-soluble salts. The washing was repeated until the pH of the supernatant became close to neutral. Finally, the MXene was separated from the suspension by vacuum filtration and dried in a vacuum oven at 80°C overnight.

1.2.3 Synthesis of sodium intercalated MXene (Na^+-MXene)

The MXene (1.00 g) was dispersed in an aqueous NaOH solution (100 mL, 3 mol/L) and stirred for 24 h at 30°C. The obtained product was sonicated for 30 min in a bath sonicator and then homogeneously mixed by a mechanical vortex. The suspension was centrifuged (3,500 rpm, 5 min) and washed with DI water until the pH of the supernatant became neutral. The powder was collected by vacuum filtration and dried in the vacuum at 80°C overnight. The obtained black powder was designated as Na^+-MXene.

1.3 Characterization

The crystal structure was analyzed by X-ray diffractometer (Ultima IV Rigaku, Japan) using Ni-filtered Cu Kα radiation ($\lambda = 1.5406$ Å). Structural morphology was analyzed by scanning electron microscopy (SEM, SEM-JSM-6700F, JEOL Ltd.) and field emission transmission electron microscopy (FE-TEM, JEM-2100F, JEOL Ltd.). Specific surface area and pore size were evaluated by N_2 adsorption-desorption isotherms (Belsorp-mini, BEL Japan, Inc.). Zeta potential values and hydrodynamic radii were obtained by electrophoretic light scattering and dynamic light scattering methods, respectively, using an LSZ-1000 instrument (Otsuka electronics). The X-ray photoelectron spectroscopy (XPS) was carried out with a mono Al-X-ray source (K-alpha, Thermo VG, U.K.). For XPS measurement, the powder sample was condesned to a pellet in order to avoid contamination from the atmosphere. Deconvolution of the XPS spectra was done by employing "XPS PEAK 41" software using Gaussian-Lorentzian curve fitting with Shirley background. The electronic structure was estimated by ultraviolet photoelectron spectroscopy (UPS, Versaprobe II, ULVAC-PHI, Japan). The UPS samples were prepared by drop casting of suspensions on ITO substrates followed by drying in the vacuum oven. Thermal gravimetric analysis (TGA) was conducted by Pyris TGA/N-1000 (SCINCO Co., Ltd., USA). Solid state ^{23}Na magic angle spinning (MAS) nuclear magnetic resonance (NMR) spectroscopy was measured by Avance II HD (Bruker, USA) at 500 MHz with a spinning rate of 10 KHz. The spectrum was referenced to a 0.1M NaCl aq. as a 0 ppm. Attenuated total reflectance (ATR) Fourier-transform infrared spectroscopy (FT-IR) was measured by FT/IR-4600 (Jasco Corporation, Japan).

1.4 Adsorption behavior of doxorubicin

Adsorption efficiencies toward DOX for the adsorbents – MAX, the MXene, and Na$^+$-MXene – were investigated by a series of adsorption experiments. The adsorption kinetic studies were conducted for 50 mL of DOX solution (10 mg/L) by adding 10 mg of the adsorbents. At pre-determined time intervals (5 min, 10 min, 20 min, 30 min, 50 min, 120 min, and then, every 60 min until 480 min), aliquots of the suspension were taken and filtered through a 0.45 μm syringe filter and the absorbance at 485 nm of the supernatant was measured by UV-vis spectroscopy (UV-1800, Shimadzu Corporation, Japan) to determine the residual concentrations. The time profiles were fitted with *pseudo*-first order (eq. 1) and *pseudo*-second order equations (eq. 2) as follows,

$$\ln\left(q_e - q_t\right) = \ln q_e - k_1 t \qquad (1)$$

$$\frac{t}{q_t} = \frac{1}{k_2 q_e^2} + \frac{t}{q_e} \qquad (2)$$

Where, k_1: *pseudo*-first-order rate constant (min^{-1}), k_2; *pseudo*-second-order rate constant (g mg^{-1} min^{-1}), q_e and q_t: the adsorbed amount of DOX (mg g^{-1}) at equilibrium and at time t (min), respectively.

In the adsorption isotherm study, DOX solutions with a concentration of 10-1000 mg/L were used. The removal efficiency ($R\%$) and adsorbed amount at equilibrium (q_e) were calculated by using the initial concentrations (C_o) and equilibrium concentrations (C_e) of DOX by using equations (S1) and (S2). All the experiments were conducted in the dark to avoid photodegradation of DOX. The experiments were done in triplicate and average values with the relative standard deviation were used. The adsorption isotherms were analyzed by Langmuir (3) and Freundlich equations (4)

$$R\% = \frac{C_o - C_e}{C_o} \times 100 \qquad (S1)$$

$$q_e = \frac{(C_o - C_e)}{m} \times V \qquad (S2)$$

$$\frac{C_e}{q_e} = \frac{1}{q_m K_L} + \frac{C_e}{q_m} \qquad (3)$$

$$\ln q_e = \ln K_F + \frac{1}{n} \times \ln C_e \qquad (4)$$

Where, m: the mass of the adsorbent (g), V : the total volume of the suspensions (L), q_e: amount of DOX adsorbed at equilibrium (mg g^{-1}), T: temperature (K), K_L: Langmuir constant (L mol^{-1}), q_m: maximum adsorption capacity (mg g^{-1}), K_F : Freundlich constant (mg g^{-1} L^{n} mol^{-n}), and n: Freundlich exponent, respectively.

The pH dependent adsorption of DOX was examined at different pH values of 2, 4, 6, 7, 8, and 10. The adsorbent (10 mg) was added to DOX solutions (10 mL, 11 mg/mL) and the suspensions were stirred for 24 h in the dark. The adsorbed amount was estimated by the same protocol as the kinetic study. Temperature dependence of DOX adsorption was investigated at 298, 306, 312, and 328 K. The adsorbents (10 mg) were dispersed in the DOX solution (10 mL, 22 mg/mL) and stirred for 24 h. The adsorbed amount was estimated by the same protocol as the kinetic study. Standard enthalpy change (ΔH^0, kJ mol^{-1}) and standard entropy change (ΔS^0, JK^{-1} mol^{-1}) were estimated from Van't Hoff equation (eq 7). Standard Gibbs free energy change (ΔG^0, kJ mol^{-1}) was estimated from thermodynamic equilibrium constant ($K_c = q_e/C_e$, as shown in eq 5) and general gas constant R (= 8.314 J mol^{-1} K^{-1}) as shown in eq. 6.

$$lnK_c = \frac{\Delta S^0}{R} - \frac{\Delta H^0}{RT} \tag{5}$$

$$\Delta G^0 = -RTlnK_c \tag{6}$$

1.5 Adsorption selectivity

The adsorbed amount of DOX on Na$^+$-MXene was compared with another organic moieties such as rhodamine 6G (Rh 6G), rhodamine B (Rh B) and Safranin O (SO). The Na$^+$-MXene was added to the solutions of solutions containing each organic moiety with an initial concentration of

10 mg/L. The suspensions were stirred for 24 h, and then filtered. The adsorbed amount of each dye was estimated by UV-vis absorption spectra.

1.6 Monte-Carlo simulation

In order to probe the adsorption mechanism occurring on the surface of MXene slabs, Monte Carlo simulations were performed using SORPTION code (available in Materials Studio, Biovia). When performing Monte Carlo calculations, it is possible to extract different information concerning the energy and the configuration of the adsorbate on the surface of the solid.

In our study, we investigated MXene structures. For that purpose, different slabs have been built. Starting from the MXene crystal structure, slabs were defined according to the plane (0 0 -1) in Materials Studio to define a slab parallel to the layer. Then to assure the electroneutrality of the structure, OH group were added close to C or Ti and the resulting structures were optimized by Forcite (Materials Studio, Biovia), by keeping the cell parameters fixed and using the universal force field (UFF) and charges calculated from the qEq method. The Ewald summation was considered for calculating electrostatic interactions while short-range interactions were evaluated using a cut-off distance of 12 Å. The convergence criteria were set at: 1.0 × 10−4 kcal mol^{-1} (energy), 0.005 kcal mol^{-1} $Å^{-1}$ (forces), and 5.0 × 10^{-5} Å (displacement). All geometry optimizations converged to provide a plausible crystallographic structure for each MXene slabs investigated in this paper. The unit cell for a slab built using at least 3 layers of MXenes, considering the experimental distances but without taking into account the hydration between layers. In addition, the MXene layers were considered as perfect, it means without impurity (Al, F,…) and the groups present in the surface are either OH or ONa and not a possible mixture, due to the fact that the multicell to consider would be too large for the calculations.

Regarding the MXenes slabs and adsorbates molecules, geometry optimization procedures were followed to extract the partial charges from DMol^3 from Materials Studio using the Mulliken repartition procedure. For the convergence, energy convergence, gradient convergence and displacement convergence were fixed at 10^{-5} Ha, $2 \cdot 10^{-3}$ Ha/Å and $5 \cdot 10^{-3}$ Å, respectively. The results were reported on Figure S23 for adsorbates.

For the solids:

- OH-saturated MXene slabs (left OH close to C and right OH close to Ti):

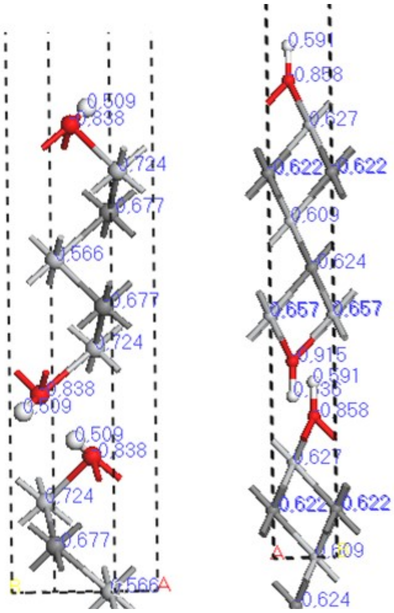

- ONa-saturated MXene slabs (left ONa close to C and right ONa close to Ti): the partial charges for Na+ were fixed at 1 to allow the exchange with +1 charged adsorbates such as DOX$^+$ (containing a NH_3^+).

Monte Carlo simulations were performed, typically with 2.0×10^6 Monte Carlo steps for equilibration, followed by 5×10^6 steps for production. The Ewald summation was also used for calculating electrostatic interactions while short-range contributions were computed with a cut-off distance of 12 Å. The simulations were conducted at 300 K using the previously simulated structures considered as rigid and with cell parameters allowing for the use of a 12 Å cut-off distance (multicells were considered with 20 x 10 x 1 slab unit cells). Again, a UFF force field was used in regard to the MXene framework atoms and adsorbate molecules (SO, Rh 6G, DOX and DOX^+). From the calculations, molecular configurations on the MXene surfaces and adsorbate molecules were obtained and discussed in the paper as well as the adsorption energy corresponding to the energy of interaction between adsorbate and the surface.

2. XRD patterns

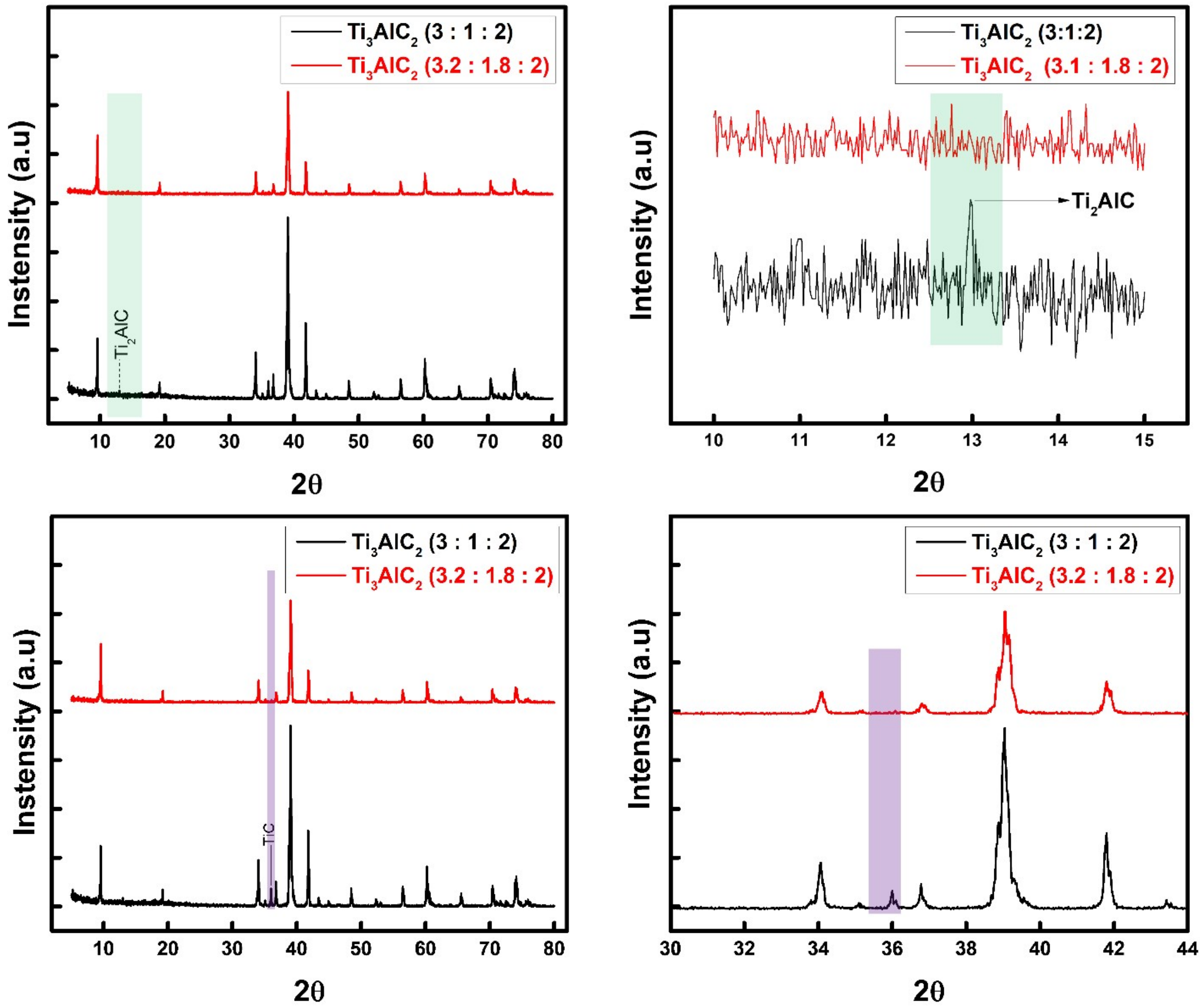

Fig. S1. XRD patterns of the MAX synthesized by stoichiometric ratios of Ti: Al: C = 3: 1: 2 and 3.2: 1.8: 2.

The powder synthesized with the ratio of Ti: Al: C = 3: 1: 2 showed peaks corresponding to unintended impurities of Ti_2AlC ($2\theta = 13°$) and TiC (35.91° and 41.75°) as shown in Fig. S1. The generation of the impurities was thought to be due to the evaporation of Ti and Al at the reaction temperature of 1450°C due to the evaporation temperature of Al (1100°C) [1] and Ti (1377°C)[2], respectively. In this regard, the stoichiometric ratio was adjusted by increasing Al and Ti sources (Ti: Al: C= 3.2: 1.8: 2) to obtain the pure phase, resulting in a single phase of Ti_3AlC_2 as shown in Fig. 2a in the main manuscript.

3. SEM images

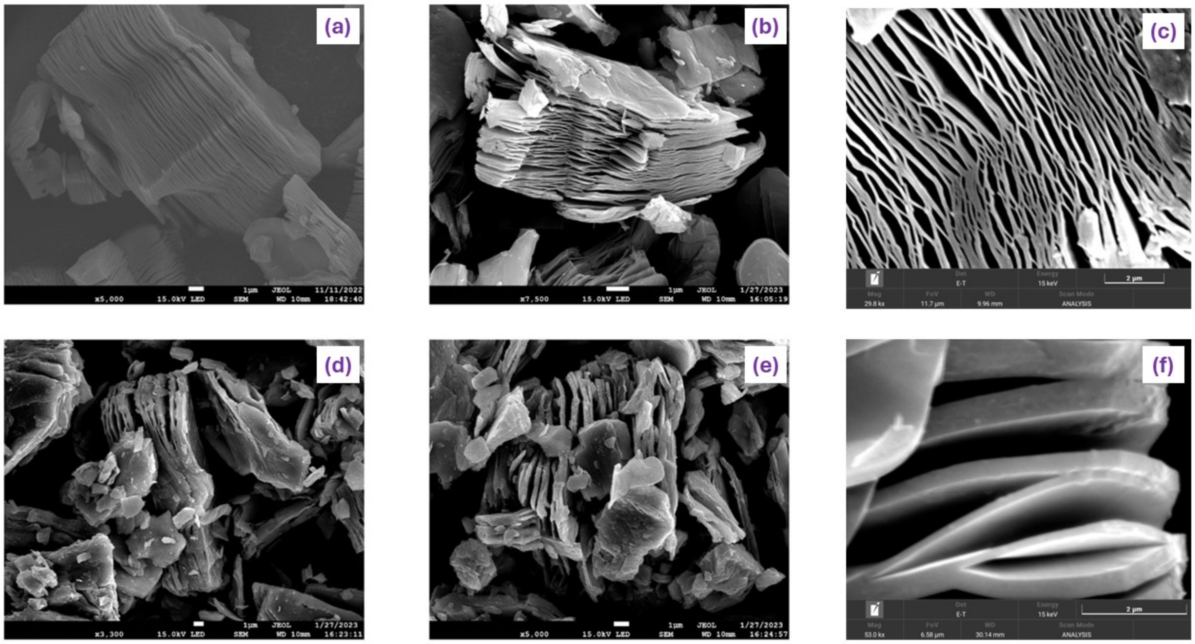

Fig. S2. SEM images of MXene (a,b,c) and Na^+-MXene (d,e,f).

4. Energy dispersive spectroscopy (EDS) elemental mapping

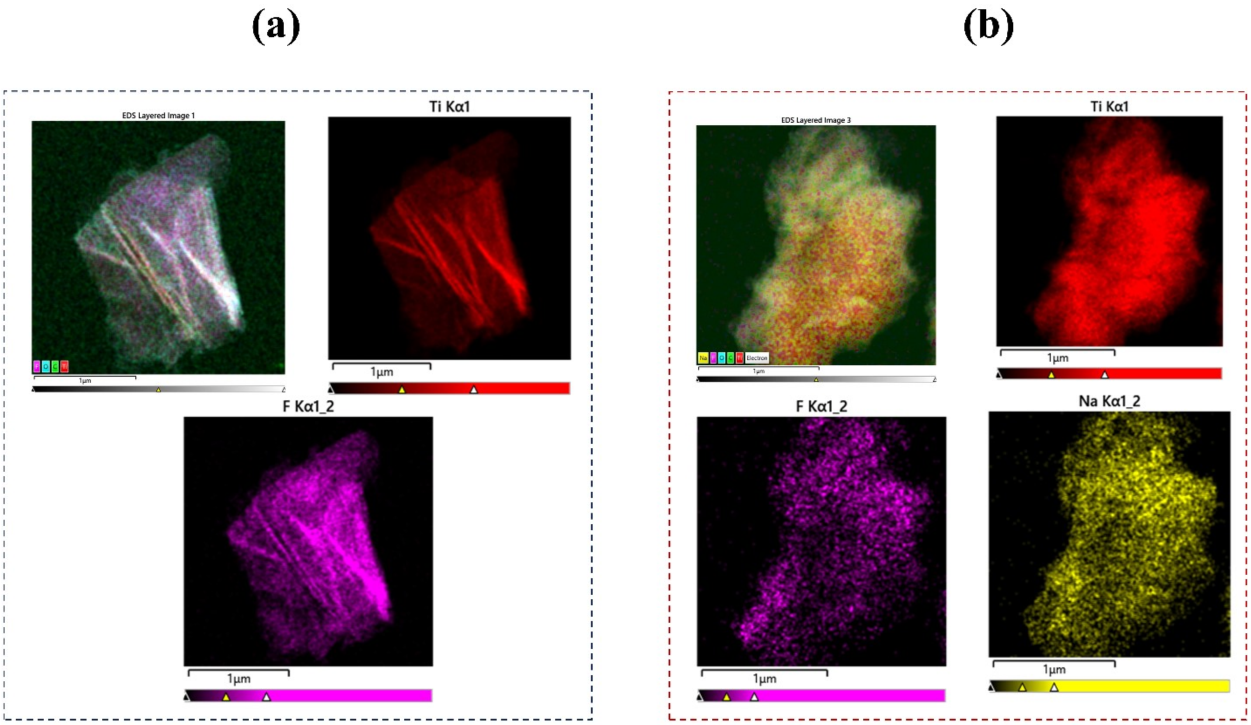

Fig. S3. EDS elemental mapping of the MXene (a) and Na$^+$-MXene (b).

5. N_2 adsorption-desorption isotherms

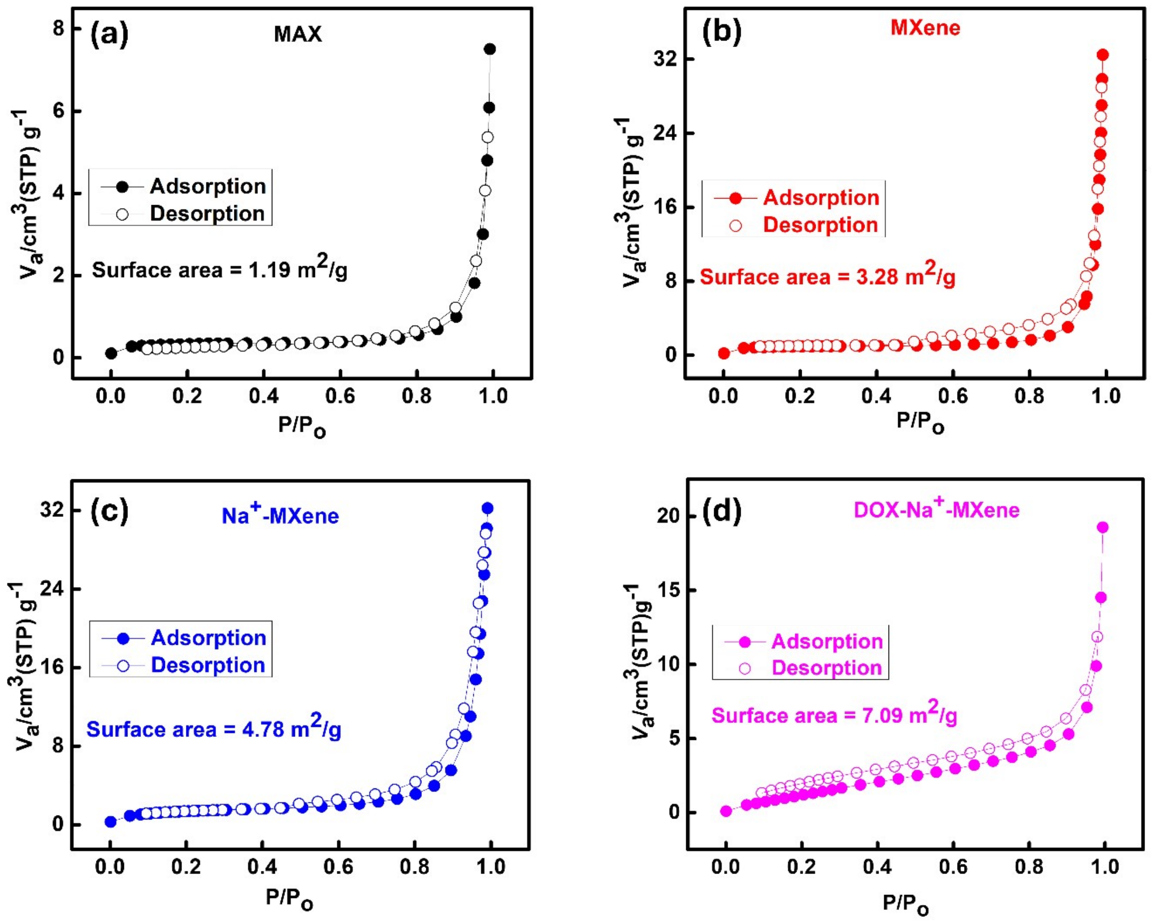

Fig. S4. N_2 adsorption-desorption isotherms of (a) MAX, (b) MXene, (c) Na^+-MXene, and (d) DOX-Na^+-MXene.

6. XPS spectra

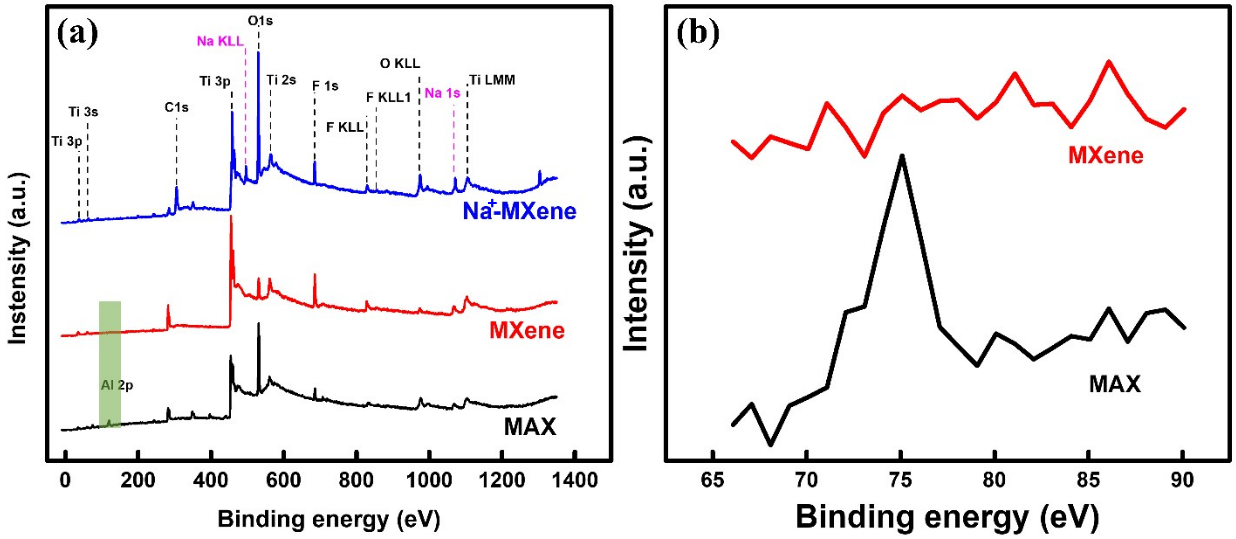

Fig. S5. XPS survey spectra of (black line) the MAX, (red line) the MXene, and (blue line) Na^+-MXene (a) and magnified spectra in Al2p region for confirmation of removal of Al from MAX (b).

XPS spectra for F 1s[3]

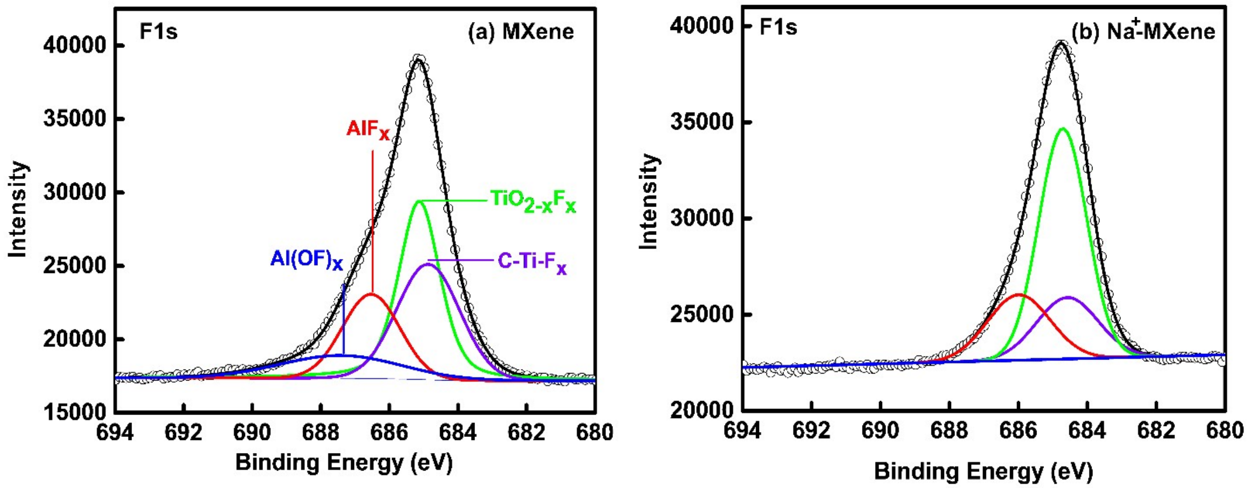

Fig. S6. XPS spectra of F of (a) MXene and (b) Na$^+$-MXene.

XPS spectra for O1s

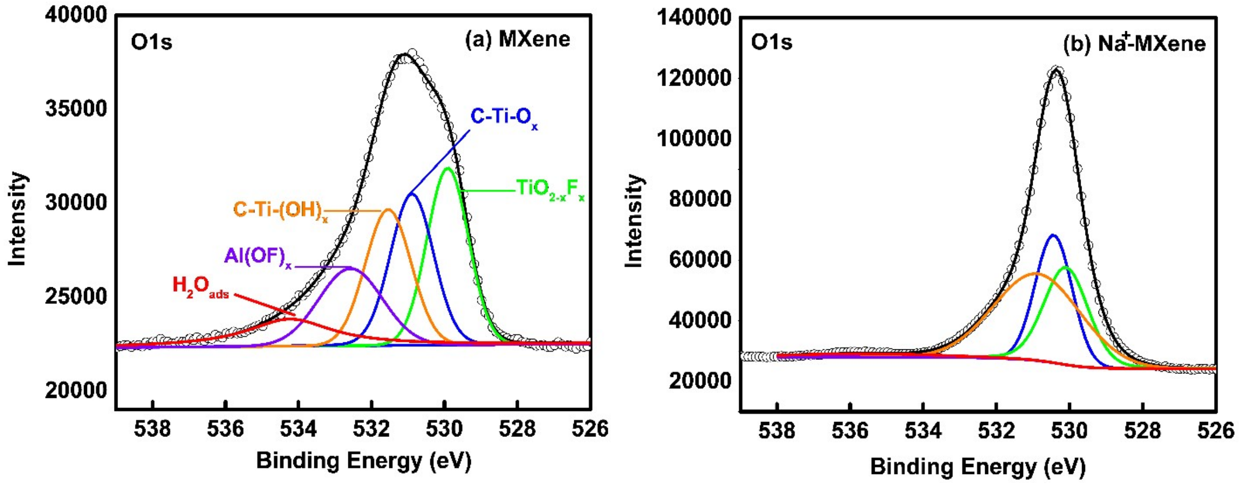

Fig. S7. XPS spectra of O1s of (a) MXene and (b) Na$^+$-MXene.

XPS spectra for O 1s for both the MXene and Na^+-MXene showed each one peak at 531.09 eV and 530.37 eV, respectively (Fig. S6c and d). The peaks were further deconvoluted to five components corresponding to $TiO_{2-x}F_x$, C–Ti–O_x, C–Ti–$(OH)_x$, $Al(OF)_{x,}$ and adsorbed water (H_2O_{ads}) which includes intercalated water[3–5], respectively. As it can be clearly observed in Fig. S6d, the intensity of C–Ti–$(OH)_x$ increased in Na^+-MXene, suggesting that the increment in the OH terminations. The photoelectron intensity from $TiO_{2-x}F_x$ related to the surface vacancy of Na^+-MXene increased compared to that of the MXene, which corresponded to the spectrum for F 1s and Ti 2p. The peak attributable to H_2O_{ads} was not observed in Na^+-MXene. Thanks to the wider interlayer distance and the larger number of the O-type surface groups of Na^+-MXene than those of the MXene, the water molecules in/on Na^+-MXene are thought to move relatively freely compared to the MXene to lower binding energy. Furthermore, the ^{23}Na NMR suggested the intercalated Na had several hydration states. Taking into these aspects, it was thought that H_2O_{ads} in Na^+-MXene had several chemical environments to show smaller with broader peak. It might be a reason for the disappearance of the peak.

XPS spectra for C1s

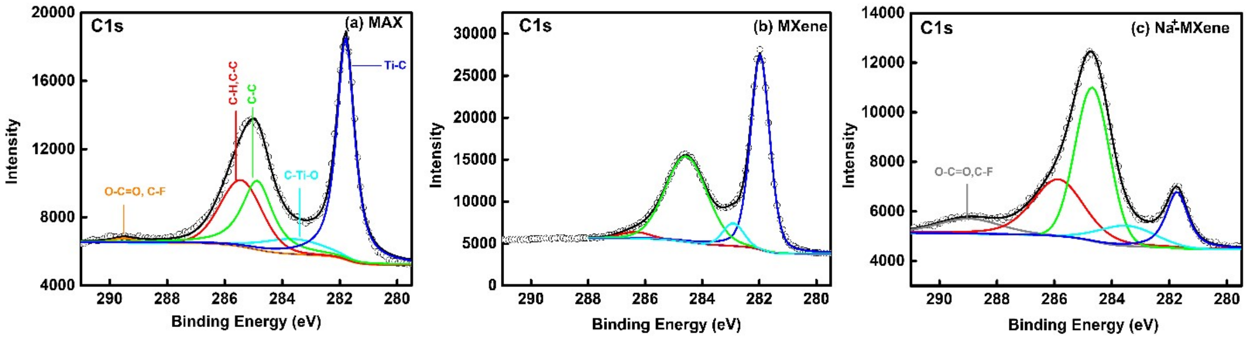

Fig. S8. XPS spectra of C1s of (a) MAX, (b) MXene, and (c) Na^+-MXene.

XPS spectra for Al 2p[6,7]

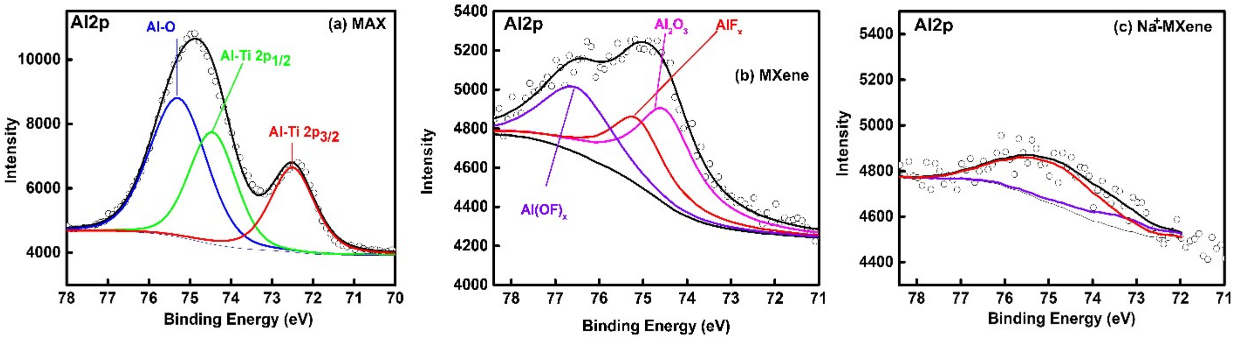

Fig. S9. XPS spectra of Al2p of (a) MAX, (b) MXene, and (c) Na$^+$-MXene

XPS spectrum for Na1s

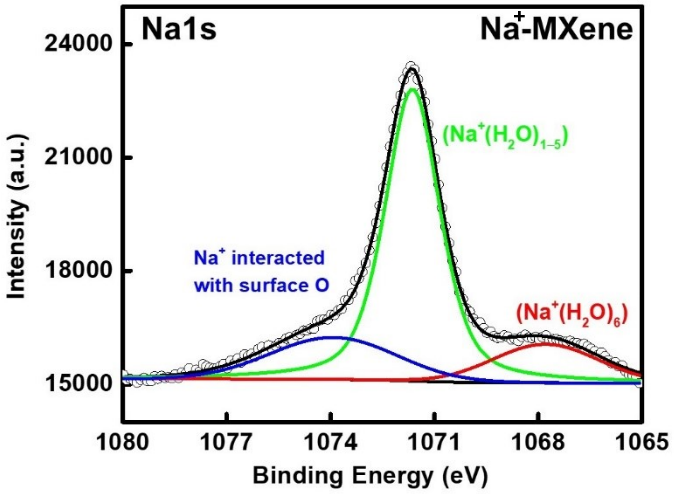

Fig. S10. XPS spectrum of Na1s of Na$^+$-MXene.

The Na 1s spectrum of Na^+-MXene showed two peaks at 1071.67 eV and 1067.68 eV which were deconvoluted to three peaks. From the similarity to a K intercalated MXene,[8] the two deconvoluted peaks at 1073.90 eV and 1071.65 eV implied Na salt such as NaF, although the low contents of F in Na^+-MXene (Table 2 in the main manuscript) suggests that the intercalated Na^+ was in the several chemical environment due to the heterogeneous surface of Na^+-MXene.

XPS spectra for O1s

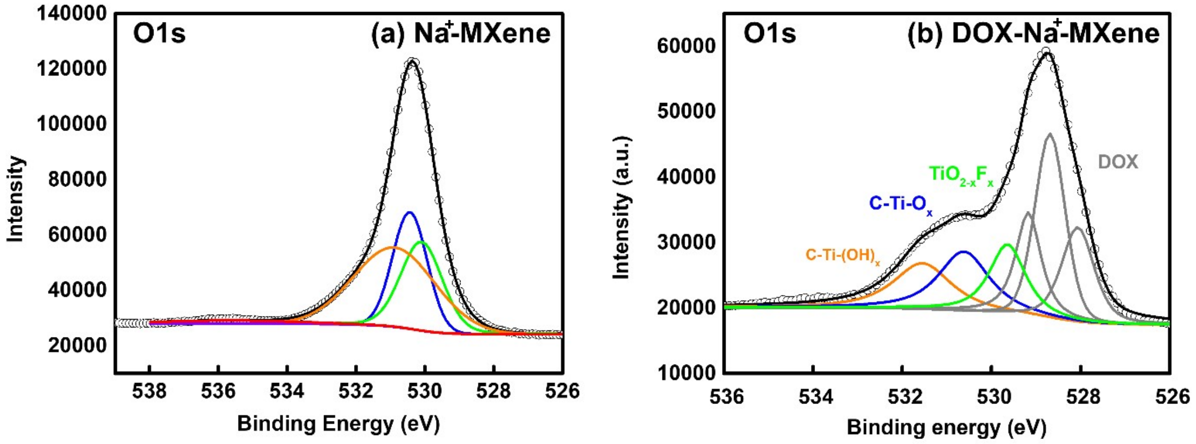

Fig. S11. XPS spectra of O1s of (a) Na^+-MXene (b) DOX-Na^+-MXene.

XPS spectra for C1s

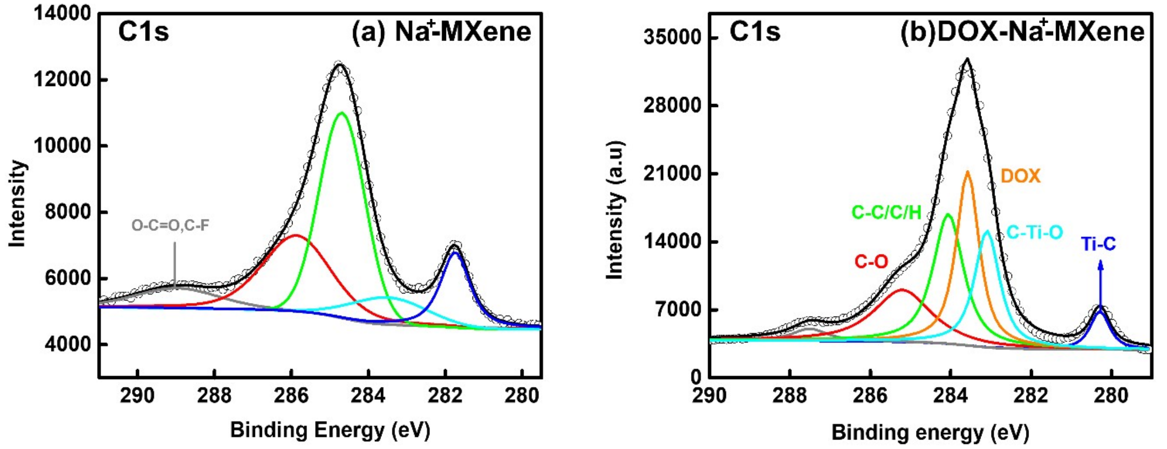

Fig. S12. XPS spectra of C1s of (a) Na^+-MXene (b) DOX-Na^+-MXene.

XPS spectra for Na1s

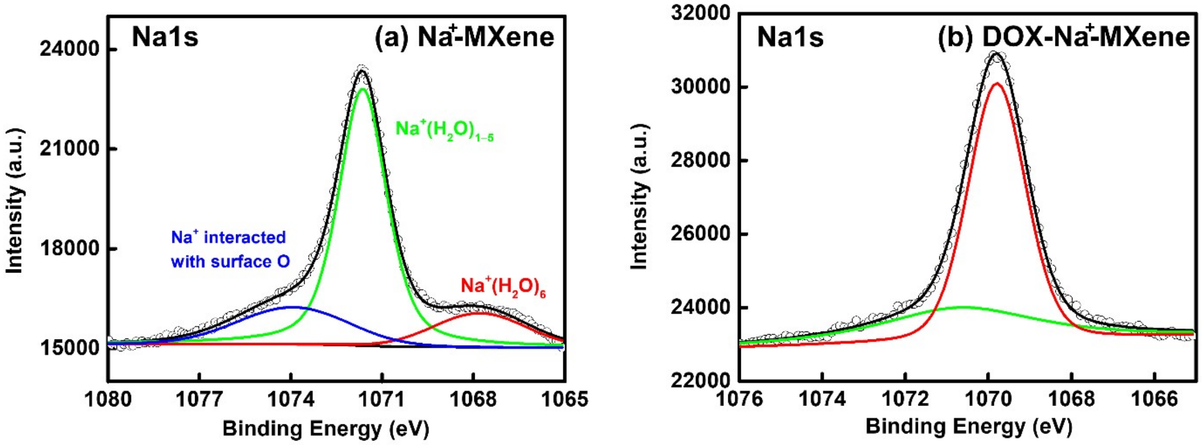

Fig. S13. XPS spectra of Na 1s of (a) Na^+-MXene (b) DOX-Na^+-MXene.

7. TGA

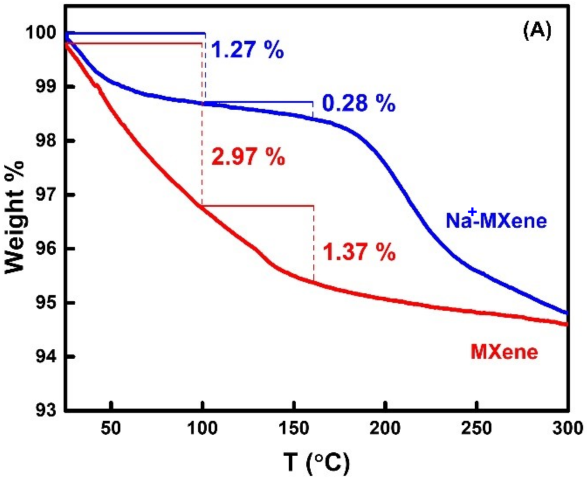

Fig. S14. TGA curves of the MXene and Na^+-MXene.

8. ^{23}Na NMR

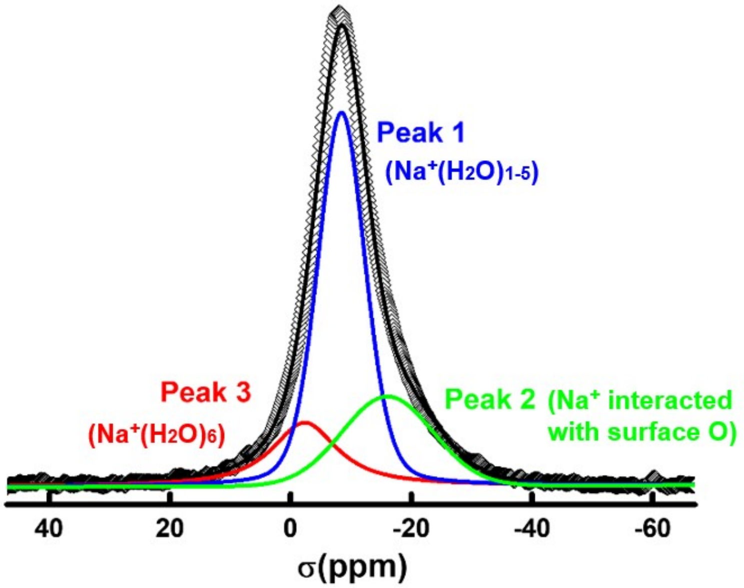

Fig. S15. ^{23}Na solid-state NMR spectrum of Na$^+$-MXene.

Table S1. Full width at half maximum (FWHM) value of deconvoluted NMR peaks (Fig. S15).

	FWHM		
Na$^+$-MXene	Peak 1	Peak 2	Peak 3
	9.51	17.77	14.61

9. Zeta Potential and Dynamic light scattering

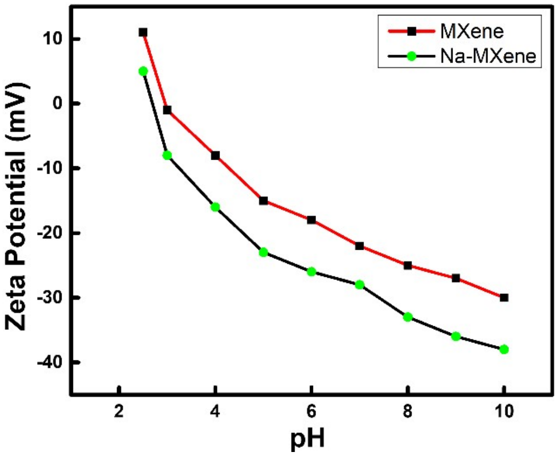

$^+$

	Isoelectric point
MXene	2.95
Na$^+$-MXene	2.69

Fig. S16. pH-dependent zeta potential of MXene.

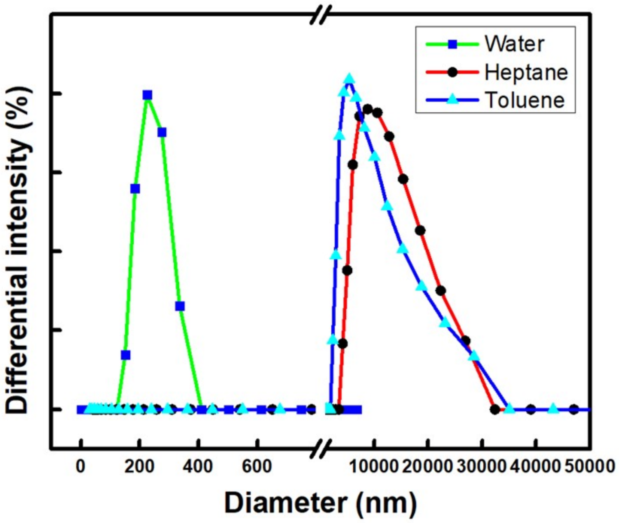

	Hydrodynamic radius (nm)
Water	242
heptane	5397
toluene	8665

Fig. S17. DLS of Na$^+$-MXene in water, heptane, and toluene.

10. Pseudo-first order and pseudo-second order fittings

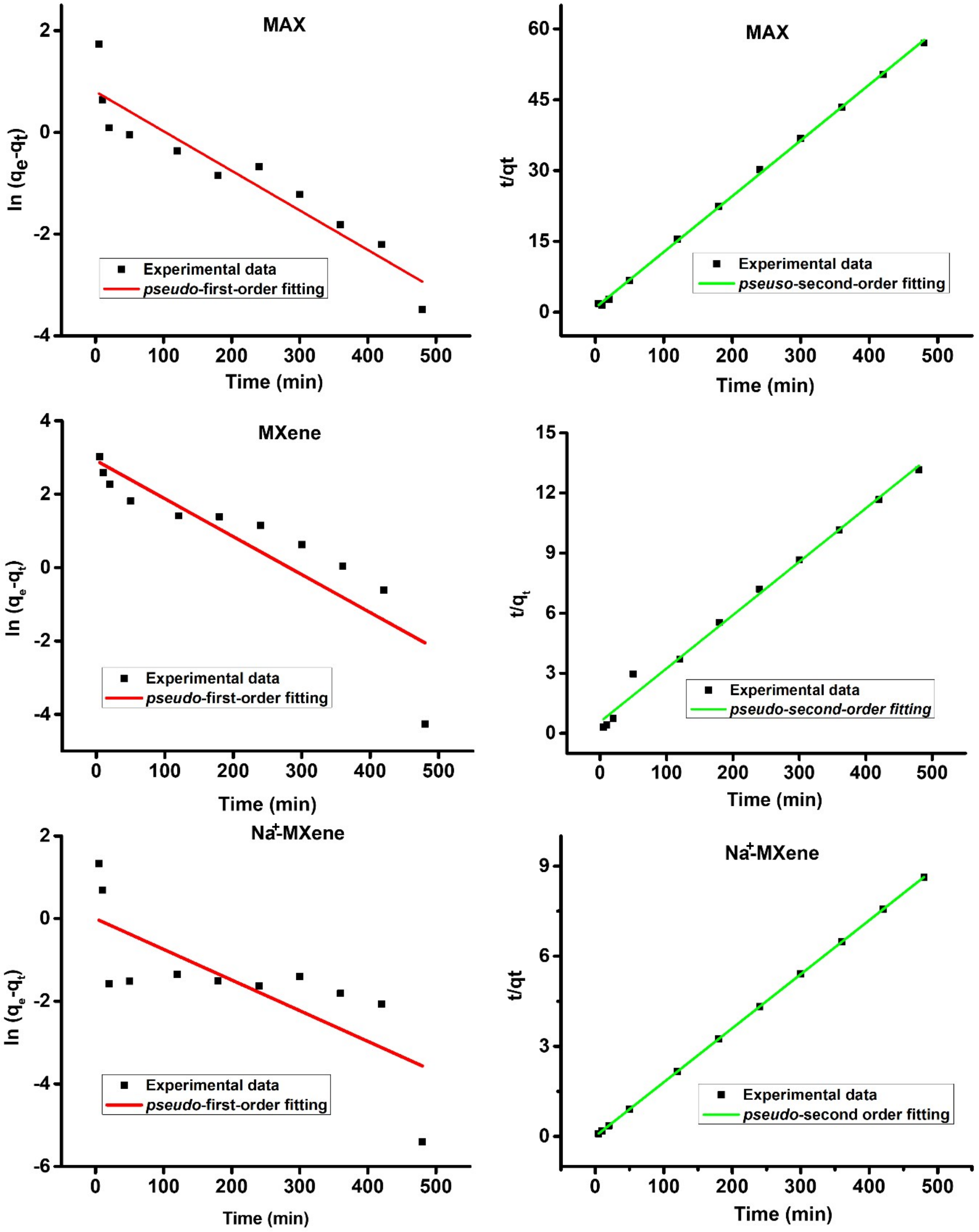

Fig. S18. *pseudo*-first-order and *pseudo*-second-order fittings for DOX adsorption on the MAX, the MXene, and Na^+-MXene.

Table S2. Kinetics parameters obtained for adsorption of DOX on the MAX, the MXene, and Na^+-MXene.

	***pseudo*-first order**		***pseudo*-second order**	
	k_1 (min^{-1})	**R^2**	**k_2 ($g\ mg^{-1} min^{-1}$)**	**R^2**
MAX	0.0033	0.87	0.0149	0.99
MXene	0.0044	0.77	0.00124	0.99
Na^+-MXene	0.0032	0.53	0.0476	0.99

11. Langmuir and Freundlich fittings

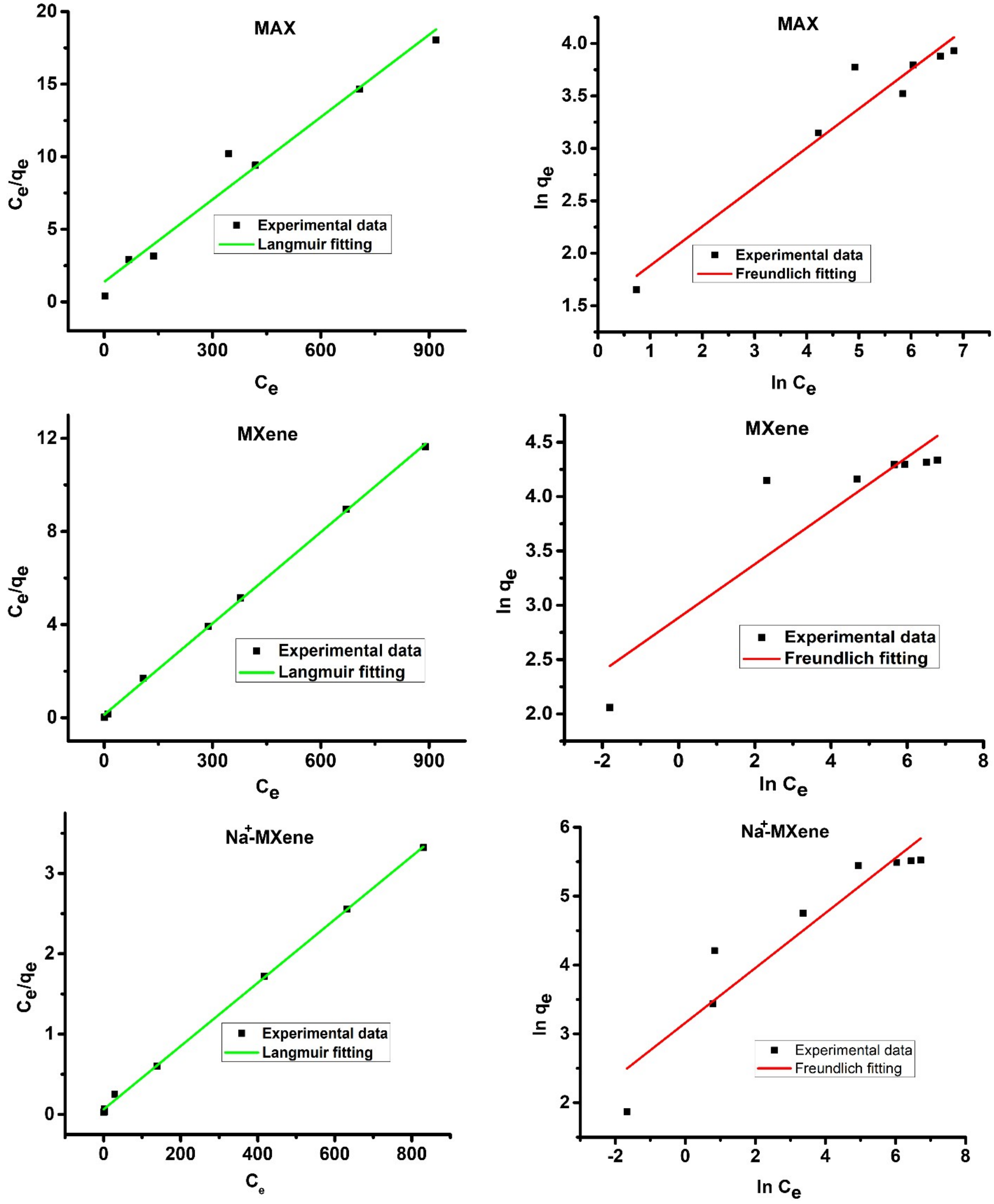

Fig. S19. Linear fitting of Langmuir and Freundlich models for the MAX, the MXene, and Na^+-MXene.

12. Van’t Hoff plot

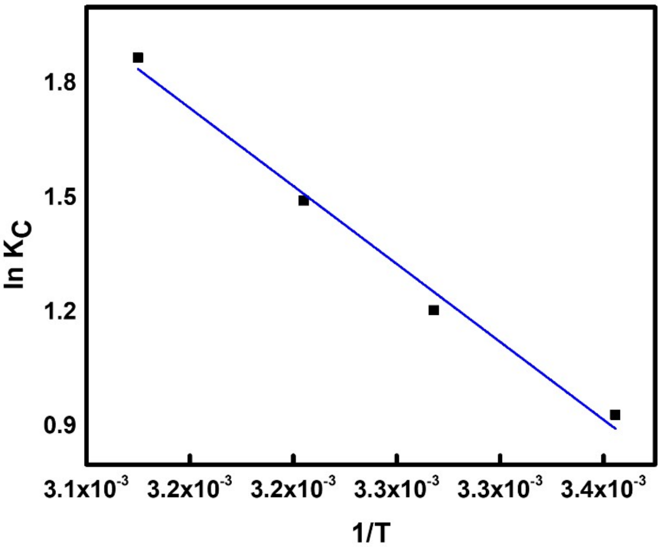

Fig. S20. Van't Hoff plot for DOX adsorption on Na$^+$-MXene.

13. UPS spectra and work function

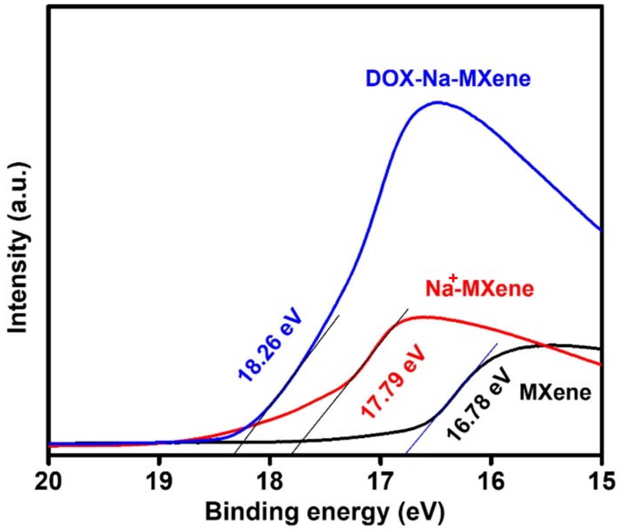

Fig. S21. UPS spectra of MXene, Na$^+$-MXene, and DOX-Na$^+$-MXene around secondary electron cut-off measured by He I (*hv* = 21.22 eV).

Table S3. Work function of MXene, Na$^+$-MXene, and DOX-Na$^+$-MXene calculated by subtracting the secondary electron cut-off from the excitation energy (*hv* = 21.22 eV)

	Work function (eV)
MXene	4.44
Na$^+$-MXene	3.43
DOX-Na$^+$-MXene	2.96

14. FT-IR spectra

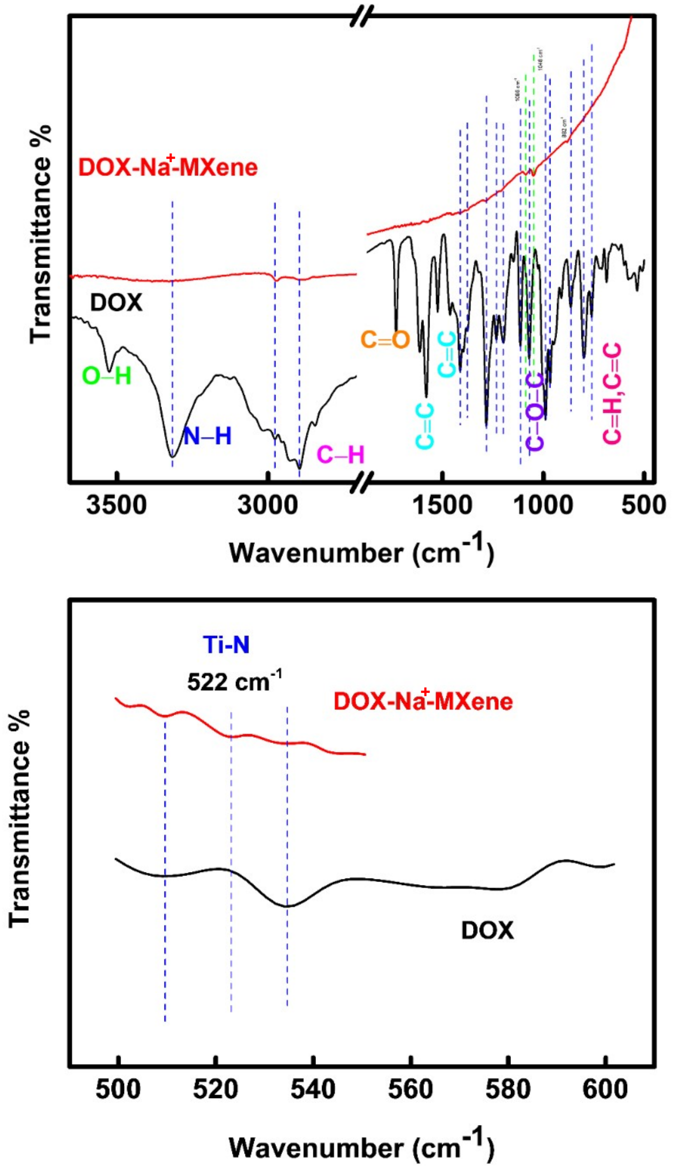

Fig. S22. IR spectra of DOX before and after adsorption on Na^+-MXene.

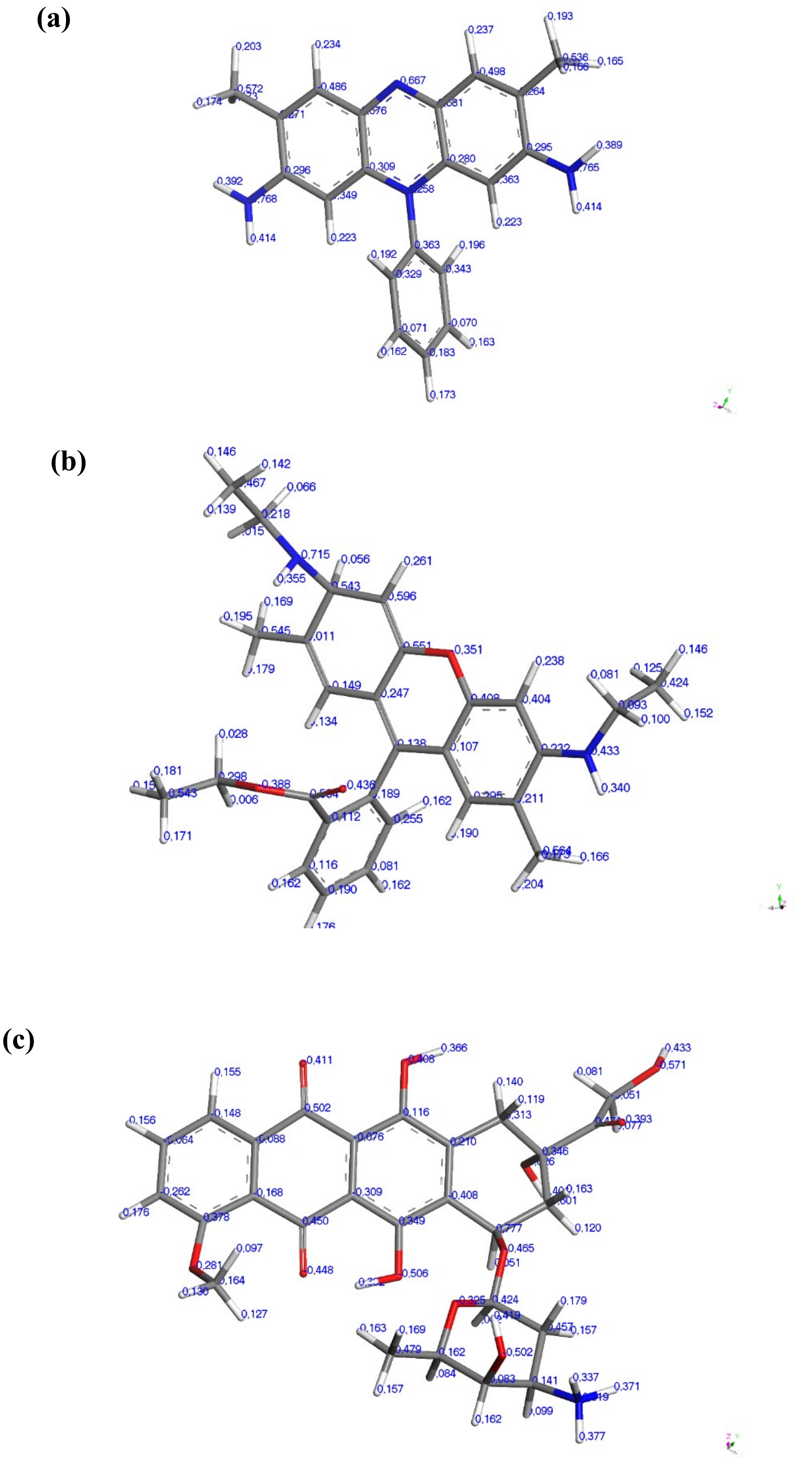

Fig. S23. Partial charges for (a) SO, (b) Rh 6G, and (c) DOX^{+}.

16. Comparison of adsorption capacity of DOX by adsorbents in the previous study

Table S4. Comparison of the adsorption capacity of DOX by different adsorbents.

Adsorbent	pH	Adsorption capacity (mg/g)	Reference
C-Fe_3O_4@ZIF-8	-	133.33	9
Fe_3O_4 NPs	6.0	106.3	10
Fe_3O_4@SiO_2-Glu	7.4	71.94	11
PVA coated Fe_3O_4	-	58	12
MCM-41-type silica	7	56.77	13
Magnetite nanospheres	7	17.55	14
Ti_3C_2@Fe_3O_4@β-CD	7	7.35	15
Lumira granular aerogel	6.5-7	13.80	16
Fe_3O_4@SiO_2/ZIF-67	4-8	90.7	17
Mango seed activated carbon	5	135.8	18
GO-CS	6.3	4.44	19
Ti_3C_2-SL	7	190.78	20
GO@Fe_3O_4@β-CD	-	204.5	21
GO-CeO_2	8.3	10.09	22
$Bi_{1-x}La_xFeO_3$	7	163.39	23
Fe_3O_4/Al_2O_3/C	5	39.25	24
Hydrazone-linked COFs	7	137.4	25
Ti-MOF@TiO_2@WMPB@CTH	6	46.11	26
NIC	9	128	27
Polysulfone/MIL-125-NH_2 (Ti)	8	24.3	28

Carbonized FeNPs@ZIF-8	7	133.3	[29]
MSAC@GE-SA	7	239.4	[30]
Sulfonated Azocalix[4]arene MOF	7	122.1	[31]
Acid-treated activated carbon	8	128.2	[32]
Acid-treated Na-Montmorillonite	7	105.3	[32]
MAX	**7**	**50.9**	**This work**
MXene	**7**	**76.40**	**This work**
Na^+-MXene	**7**	**250**	**This work**

17. References

1. Wang, W. *et al.* Effect of Al evaporation temperature on the properties of Al films grown on sapphire substrates by molecular beam epitaxy. *RSC Adv.* **5**, 29153–29158 (2015).

2. a:: / { (1 -. 4144 (1949).

3. Halim, J. *et al.* X-ray photoelectron spectroscopy of select multi-layered transition metal carbides (MXenes). *Appl. Surf. Sci.* **362**, 406–417 (2016).

4. Pazniak, A. *et al.* Ti3C2Tx MXene characterization produced from SHS-ground Ti3AlC2. *Mater. Des.* **183**, 108143 (2019).

5. Halim, J., Persson, I., Eklund, P., Persson, P. O. A. & Rosen, J. Sodium hydroxide and vacuum annealing modifications of the surface terminations of a Ti3C2 (MXene) epitaxial thin film. *RSC Adv.* **8**, 36785–36790 (2018).

6. Myhra, S., Crossley, J. A. A. & Barsoum, M. W. Crystal-chemistry of the Ti3AlC2 and Ti4AlN3 layered carbide/nitride phases - characterization by XPS. *J. Phys. Chem. Solids* **62**, 811–817 (2001).

7. Abdul, A. *et al.* Adsorption and electrochemical regeneration of intercalated Ti 3 C 2 T x MXene for the removal of ciprofloxacin from wastewater. *Chem. Eng. J.* **421**, 127780 (2021).

8. Dall'Agnese, Y. *et al.* High capacitance of surface-modified 2D titanium carbide in acidic electrolyte. *Electrochem. commun.* **48**, 118–122 (2014).

9. Cai, W., Ye, Y., Weng, X., Owens, G. & Chen, Z. Mechanistic insight into loading of doxorubicin hydrochloride onto carbonized FeNPs@ZIF-8 composite. *Sep. Purif. Technol.* **314**, 123580 (2023).

10. Weng, X. *et al.* Removal of doxorubicin hydrochloride using Fe3O4 nanoparticles synthesized by euphorbia cochinchinensis extract. *Chem. Eng. J.* **353**, 482–489 (2018).

11. Cai, W., Guo, M., Weng, X., Zhang, W. & Chen, Z. Adsorption of doxorubicin hydrochloride on glutaric anhydride functionalized Fe 3 O 4 @SiO 2 magnetic nanoparticles. *Mater. Sci. Eng. C* **98**, 65–73 (2019).

12. Kayal, S. & Ramanujan, R. V. Doxorubicin loaded PVA coated iron oxide nanoparticles for targeted drug delivery. *Mater. Sci. Eng. C* **30**, 484–490 (2010).

13. Roik, N. V., Belyakova, L. A. & Dziazko, M. O. Adsorption of antitumor

antibiotic doxorubicin on MCM-41-type silica surface. *Adsorpt. Sci. Technol.* **35**, 86–101 (2017).

14. Kusyak, A. *et al.* Study of the adsorption activity of Fe3O4 synthesized by the solvothermal method in relation to doxorubicin. *Appl. Nanosci.* **10**, 4923–4930 (2020).
15. Liu, D., Li, T., Sun, W., Zhou, W. & Zhang, G. Magnetic Ti3C2MXene Nanomaterials for Doxorubicin Adsorption from Aqueous Solutions: Kinetic, Isotherms, and Thermodynamic Studies. *ACS Omega* **7**, 31945–31953 (2022).
16. Prasanna, V. L., Mamane, H., Vadivel, V. K. & Avisar, D. Ethanol-activated granular aerogel as efficient adsorbent for persistent organic pollutants from real leachate and hospital wastewater. *J. Hazard. Mater.* **384**, 121396 (2020).
17. Weng, X., Chen, W., Cai, W., Owens, G. & Chen, Z. Synthesis of ferroferric oxide@silicon dioxide/cobalt-based zeolitic imidazole frameworks for the removal of doxorubicin hydrochloride from wastewater. *J. Colloid Interface Sci.* **624**, 108–120 (2022).
18. Altalhi, T. A. *et al.* Adsorption of doxorubicin hydrochloride onto thermally treated green adsorbent: Equilibrium, kinetic and thermodynamic studies. *J. Mol. Struct.* **1263**, 133160 (2022).
19. Arjmand, O., Ardjmand, M., Amani, A. M. & Eikani, M. H. Effective adsorption of doxorubicin hydrochloride on the green targeted nanocomposite. *Acta Chim. Slov.* **67**, 496–506 (2020).
20. Luo, R. *et al.* Preparation of sodium ligninsulfonate functionalized MXene using hexachlorocyclotriphosphazene as linkage and its adsorption applications. *Appl. Surf. Sci.* **602**, 154197 (2022).
21. Ghafoori, M., Cheraghi, M., Sadr, M. K., Lorestani, B. & Sobhanardakani, S. Magnetite graphene oxide modified with β-cyclodextrin as an effective adsorbent for the removal of methotrexate and doxorubicin hydrochloride from water. *Environ. Sci. Pollut. Res.* **29**, 35012–35024 (2022).
22. Abbasi, M. A. *et al.* Synergetic effect of adsorption-photocatalysis by GO−CeO2nanocomposites for photodegradation of doxorubicin. *J. Environ. Chem. Eng.* **10**, (2022).
23. Abbasi, M. A. *et al.* Phase pure synthesis of lanthanum doped bismuth ferrite nanostructures for the adsorption of doxorubicin. *Ceram. Int.* **47**, 14390–14398 (2021).

24. Kusyak, N. V. *et al.* Adsorption of doxorubicin on the surface of magnetically sensitive nanocomposite Fe3O4/Al2O3/C. *Mol. Cryst. Liq. Cryst.* **751**, 10–27 (2023).

25. Ji, S. L., Xiao, S. S., Wang, L. L. & Wang, Q. P. Synthesis of hydrazone-linked covalent organic framework for pH-mediated adsorption and removal of doxorubicin hydrochloride. *Eur. Polym. J.* **201**, 112572 (2023).

26. Mahmoud, M. E. & Ibrahim, G. A. A. Cr(VI) and doxorubicin adsorptive capture by a novel bionanocomposite of Ti-MOF@TiO2 incorporated with watermelon biochar and chitosan hydrogel. *Int. J. Biol. Macromol.* **253**, 126489 (2023).

27. Olusegun, S. J. *et al.* Removal of doxorubicin hydrochloride and crystal violet from aqueous solutions using spray-dried niobium oxide coated with chitosan-activated carbon: Experimental and DFT calculations. *Int. J. Biol. Macromol.* **266**, (2024).

28. Rad, L. R., Irani, M. & Anbia, M. Membrane filtration and adsorption of doxorubicin hydrochloride and fluoxetine hydrochloride from water using polysulfone/MIL-125-NH2 (Ti) nanofibrous membranes. *J. Mol. Liq.* **408**, 125429 (2024).

29. Cai, W., Ye, Y., Weng, X., Owens, G. & Chen, Z. Mechanistic insight into loading of doxorubicin hydrochloride onto carbonized FeNPs@ZIF-8 composite. *Sep. Purif. Technol.* **314**, 123580 (2023).

30. Devre, P. V. & Gore, A. H. Agro-Waste Valorization into Carbonaceous Eco-Hydrogel: A Circular Economy and Zero Waste Tactic for Doxorubicin Removal in Water/Wastewater. *Langmuir* **40**, 141–158 (2024).

31. Cao, X. M. *et al.* Sulfonated Azocalix[4]arene-Modified Metal–Organic Framework Nanosheets for Doxorubicin Removal from Serum. *Nanomaterials* **14**, 1–15 (2024).

32. Rezaei, N., Shahrouzi, J. R., Ebadi, A., Towfighi, F. & Moradi, F. Doxorubicin Removal from Water using Acid-treated Activated Carbon, Multi-walled Carbon Nanotubes, and Montmorillonite. *Chem. Biochem. Eng. Q.* **38**, 59–69 (2024).